Title	The Effect of base irradiation on failure behaviors of UO_2 and chromia-alumina additive fuels under simulated reactivity-initiated accidents; A Comparative analysis with FEMAXI-8
Author(s)	Udagawa Yutaka,Mihara Takeshi,Taniguchi Yoshinori,Kakiuchi Kazuo,Amaya Masaki
Citation	Annals of Nuclear Energy,139,p.107268_1-107268_9
Text Version	Accepted Manuscript
URL	https://jopss.jaea.go.jp/search/servlet/search?5067210
DOI	https://doi.org/10.1016/j.anucene.2019.107268
Right	© 2020. This manuscript version is made available under the CC-BY-NC-ND 4.0 license http://creativecommons.org/licenses/by-nc-nd/4.0/

The effect of base irradiation on failure behaviors of UO_2 and chromia-alumina additive fuels under simulated reactivity-initiated accidents: a comparative analysis with FEMAXI-8

Yutaka Udagawa*, Takeshi Mihara, Yoshinori Taniguchi, Kazuo Kakiuchi and Masaki Amaya

Nuclear Safety Research Center, Japan Atomic Energy Agency
Tokai-mura, Ibaraki-ken, 319-1195, Japan

Tel. +81-29-282-6230
Fax. +81-29-282-5429
E-mail: udagawa.yutaka@jaea.go.jp
(* Corresponding author)

Abstract

This paper reports an analysis on the base irradiation behavior of the chromia-and-alumina-doped boiling water reactor (BWR) rod irradiated to 64 GWd/t in Oskarshamn-3, Sweden, and subjected to the reactivity-initiated-accident (RIA) test OS-1, which resulted in a fuel failure due to pellet-cladding mechanical interaction at the lowest fuel enthalpy increase in all the BWR tests ever performed. The inverse calculation which utilized post-irradiation examination data as its constraint conditions revealed that the OS-1 rod had very likely experienced higher cladding stress due to higher swelling rate during base irradiation than other BWR rods subjected to previous RIA tests. Thus, the OS-1 rod was prone to experience enhanced radial-hydride formation. The significant difference in the hoop-stress of more than 50 MPa discriminates the OS-1 rod from other BWR rods and supports the interpretation that enhanced radial-hydrides formation differentiates the failure behavior observed in the test OS-1 from the previous BWR-fuel tests.

Keywords: Additive fuel, Fuel performance codes, Fuel enthalpy, Fuel failure, Pellet-cladding mechanical interaction, Reactivity-initiated accident

Abbreviations[1]

1. Introduction

A RIA experiment named Test OS-1 with a high burnup BWR fuel rod was conducted at the NSRR in 2018. Since safety assessment for BWR RIAs requires anticipating a cold zero power state at which fuel cladding tends to be more susceptible to mechanical failure, the pulse irradiation test was performed at room temperature and atmospheric pressure rather than at a high temperature and high pressure condition, which is the other alternative option at the NSRR. The fuel enthalpy targeted in the test was 287 J/g by the power pulse whose full width at half maximum was 4.4 ms [1] and pulse shape was equivalent to that reported in [2]. This resulted in PCMI failure, whose condition has been estimated to be at fuel enthalpy increase of about 160 J/g [1].

This failure limit value is not only lower than that expected from the trend formed by previous tests on BWR fuels at the NSRR but also lower than the PCMI-failure threshold currently adopted in the Japanese RIA acceptance criteria [3]. Another aspect of the OS-1 test was that it was the first RIA-simulated experiment ever performed on a rod with ADOPT^{TM} (chromia-and-alumina-doped UO_2) fuel pellets. As ADOPT^{TM} fuel has been already introduced to nuclear power plants in the world, the observed failure limit reduction could develop to a safety issue of ADOPT^{TM} fuel in the case that any dopant effect is identified as the primary cause. Otherwise it would be a more general concern of high burnup BWR fuels. Elucidation of the fuel failure phenomena observed in OS-1 has become the primary purpose of the NSRR experiment program as of 2019.

Two features of the OS-1 test fuel are currently considered possible causes of the low-enthalpy failure. Firstly, as the additives are known to change fission gas behavior significantly, it should not be excluded that such and other properties different from standard UO_2 fuels could affect the failure limit. In the case of MOX fuels, the past RIA-simulated tests provoked a discussion about the possibility of an additional PCMI-loading effect [4]. It should be emphaiszed, however, that any sign of such an ADOPT^{TM}-specific effect has not been found thus far in either on-line measurements or PIEs [1]. Another feature, noticed on the cladding side, is the clear preferential orientation of the hydride precipitates along the radial direction of the cladding tube, observed in the pre- and post-test PIEs [1]. **Figure 1** compares hydride morphologies of BWR rods subjected to the OS-1 test and a different rod with higher burnup. The deteriorating effect of radially-oriented hydride precipitates has been recognized as a general trend of Zircaloy-2 cladding and is also confirmed relevant to PCMI failure through NSRR tests on high burnup BWR fuels with RX-annealed cladding [2]. Both possibilities are to be pursued and verified through follow-up PIEs and RIA-simulated tests.

[1] RIA: reactivity initiated accident, BWR: boiling water reactor, NSRR: nuclear safety research reactor, PCMI: pellet-cladding mechanical interaction, PIE: post-irradiation examination, RX: recrystallization, HBS: high burnup structure, P/C: pellet/cladding, SSR: solid-swelling rate.

This study intends to verify the latter possibility, namely contribution of radial hydrides to PCMI failure, from another aspect. It is well known from laboratory-scale studies that radial-hydride fraction in zirconium-based-alloy cladding increases with applied-stress level in hoop direction during both precipitation and growth [5]. If the orientation of hydrides varies significantly from one high burnup BWR fuel to another, the most probable driving force of such difference is thought to be the late-stage PCMI loading during base irradiation, which should emerge after pellet/cladding-gap closure with burnup progress. Late-stage PCMI conditions were thus compared between the OS-1 rod and other BWR rods subjected to previous NSRR tests to verify the consistency between the actual fuel states and the hypothesis of radial-hydrides contribution to the OS-1 test result. FEMAXI-8 code [6, 7], the fuel performance code developed by Japan Atomic Energy Agency, was applied to the analysis. Whereas preparatory updates were made on models for a better prediction, the analysis itself was designed as an inverse calculation that utilizes available PIE data as its constraint conditions to make the analysis as reliable as possible, as described in Chapter 2. Chapter 3 summarizes and discusses the analysis results, provides some sensitivity analyses, and gives an interpretation of the OS-1 test result based on the discussion.

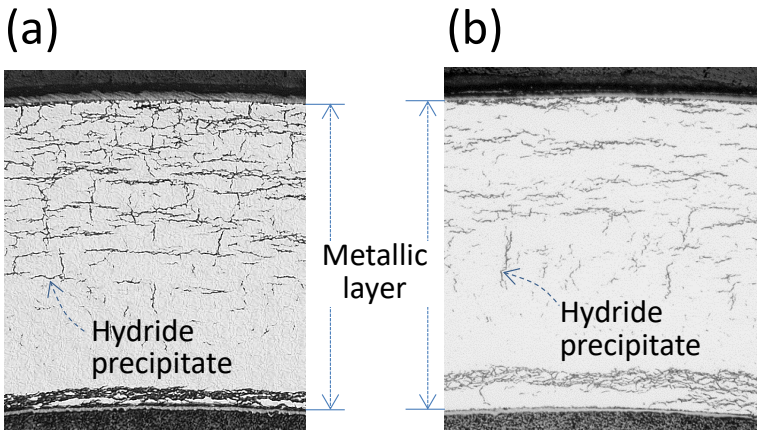

Figure 1 Cladding metallographs of mother rods (a) OS-1 (64 GWd/t) and (b) LS-1 (69 GWd/t): observation in the vicinity of each test rod position.

2. Analysis method

2.1 Calculation procedure

Figure 2 shows an outline of the present analysis. A set of analysis consists of two kinds of base irradiation calculations ((A) and (B) in the figure) by FEMAXI-8 [6, 7], each of which involves an iterative process to match a calculated parameter with a corresponding PIE result. In the first step (A), cladding oxidation rate was calibrated by comparing the calculated and measured values of oxide thickness on the cladding outer surface. In the step (B), fuel swelling rate was calibrated by comparing the calculated and measured values of the cladding outer diameter. Step (A) was necessary for accurately account for cladding corrosion effect in step (B), as cladding outer diameter is affected by both cladding corrosion and fuel swelling.

This two-step calibration procedure was applied individually to each of analyzed fuel rod. Computed cladding mechanical states such as stress and strain obtained after step (B) were subjected to comparison with other rods as a best-fit calculation result supported by the PIE data. It should be noted that step (B) was skipped in the case of overestimation, to avoid further complication of the calculation procedure. The reason and influence of such an asymmetric operation are discussed again in Section 3.1. The authors also emphasize that this kind of calibration procedure should be distinguished from a general validation approach (covered by the next section) to improve modelling of fuel behaviors. As it involves rod-by-rod parameter adjustment, model sets produced from this procedure is not expected to have improved predictive performance for blind calculations. In other words, applicability of each model set produced from the flow given in **Fig. 2** is limited to each rod whose PIE data was taken as inputs.

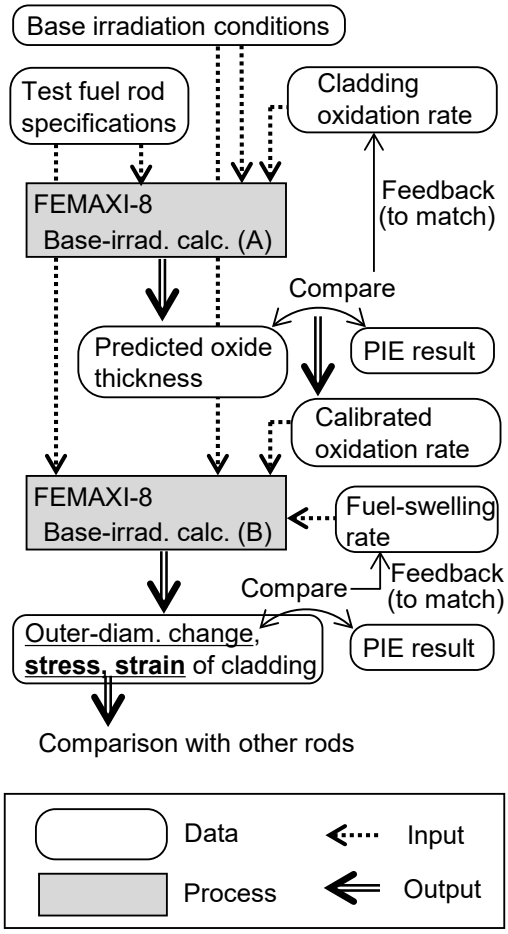

Figure 2 Inverse-calculation procedure flow chart. The data item "Base irradiation conditions" represents histories of linear heating rate, coolant pressure, and coolant inlet temperature.

2.2 Determination of calculation conditions

The present work involved preparatory model updates from recent thorough validation work [6] to facilitate the calculation procedure given in **Fig. 2**. The primary purpose of the updates was to improve predictive performance of cladding deformation during base irradiation. This

corresponds to a better starting point for the calibration process illustrated in **Fig. 2** and minimizing the necessity of rod-by-rod and manual (*i.e.*, baseless) adjustment of model parameters.

The modifications included development of a new HBS model, associated re-calibration of normal-structure fission-gas models, suppression of fuel hot-press rate, calibration of cladding creep rate, slight enhancement of fuel relocation, and change of fuel thermal-expansion models. Modifications were validated with cladding deformation data of high burnup PWR and BWR rods accumulated in the NSRR experiment database including the ALPS programs [8], while keeping the predictive performance of fuel temperature, fission-gas release, etc., achieved in the previous work [6]. **Figure 3** shows improved agreement with the PIE results by the updated model set labeled "BASE," which is the starting point for the calibration process (**Fig. 2**) in the present work. More detailed descriptions on the modifications made to the previous work [6] are described in the **Appendix**.

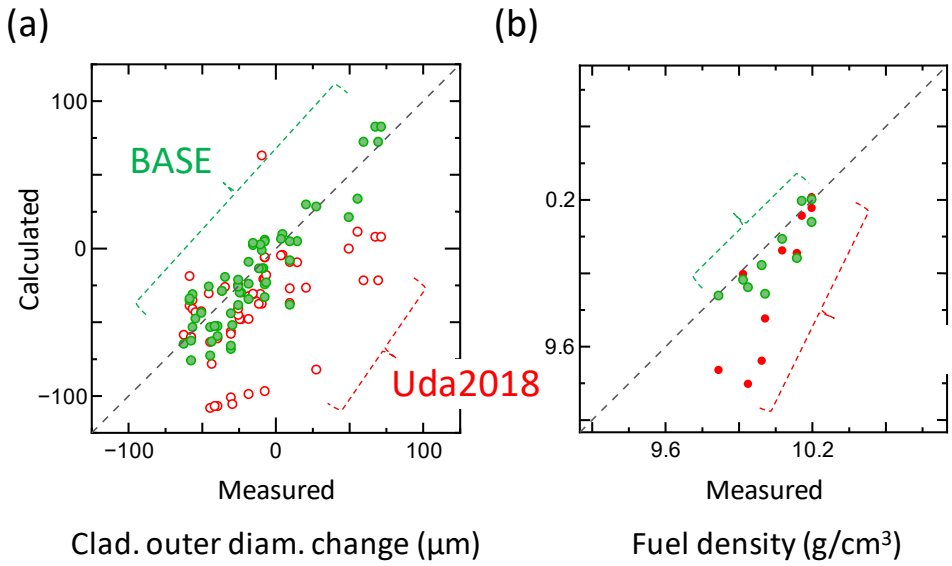

Figure 3 Comparison of (a) cladding deformation and (b) fuel density after base irradiation between calculation results and measurements for 20 PWR rods and 11 BWR rods with burnup from 26 to 84 GWd/t. Cladding deformation represents diameter change of the mother rod from its nominal value to the measured value (an averaged value for the axial range corresponding to the NSRR test rod) at the corresponding burnup. Fuel density was measured in the vicinity of the NSRR test rod section. Results labeled "Uda2018" was produced by the model set from the previous work [6] and "BASE" was produced by the model set updated in the present work.

2.3 High burnup BWR rods selected as targets of the analysis

Table 1 lists the high burnup BWR rods [1,3,9,10] which were taken from the NSRR experiment database and were selected as targets of the present analysis, namely the calculation procedure in **Fig. 2**. The burnup in these rods is higher than 50 GWd/t above which the PCMI effect is thought

to become significant due to P/C gap closure. This set of BWR mother rods include FK-6B, -8B, -10B, -13B, and LS-1B whose corresponding NSRR test rods resulted in PCMI failure until today: FK-6, -7, -8, -9, -10, -12, -13, and LS-1. The listed fuels are all sheathed with lined-Zry-2 cladding including the OS-1 rod and are all standard-UO_2 fuels except the OS-1 rod.

The adopted version of FEMAXI-8 (8.1.122z) does not support models or correlations which are specifically designed for ADOPT^{TM} fuel, but takes account of the relatively large grain size (>40 μm) and initial fuel density of around 97.4% (fractional density to the theoretical value) [11]. Grain size influences behaviors of the component models that treat fuel densification, intragranular fission gas diffusion, and intergranular fission gas migration to the free volume.

Table 1 High burnup BWR rods selected as targets of inverse calculation

Mother rod ID	Corresponding NSRR test ID	Burnup[a] (GWd/t)	Peak LHR in base irradiation[b] (kW/m)
FK-4B	FK-4, FK-5	56	~35
FK-6B	FK-6, FK-7	61	~35
FK-8B	FK-8, FK-9	61	~35
FK-10B	FK-10, FK-12	61	~35
FK-13B[c]	FK-13	59	~25
OS-1B	OS-1	64	~20
LS-1B	LS-1, LS-2, LS-3	69	~20

[a]: An averaged value for the axial range corresponding to the NSRR test rod.
[b]: An averaged value for the axial range corresponding to the whole mother rod.
[c]: The base irradiation information is available in JNES report [12].

The fuel rod was divided along the axial direction into a maximum of 12 nodes for the listed rods to treat axial power profiles. The comparison between the calculation and measurement (see **Fig. 2**) focused solely on the axial position corresponding to the NSRR test rod. For each axial node, the radial mesh number for a fuel stack is 3 for the mechanical calculation and 9 for the thermal calculation of FEMAXI-8. The radial mesh numbers are 2 for cladding base-metal layer, 2 for cladding liner-metal layer, 1 for cladding outer surface oxide layer, 1 for P/C gap, and 1 for coolant channel, applicable to both the thermal and mechanical calculations.

3. Results and discussion

3.1 Calculation results by the reference model set

Figure 4 shows how the calibration step (B) (see **Fig. 2**) influenced the predicted cladding outer diameter change of the targeted BWR rods (see **Table 1**) during their base irradiations. The points labeled "As-predicted" are a replot of those already included as the "BASE" group in **Fig. 2** for the selected BWR rods. The inverse calculation started with the "BASE" model set and finally settled in "REF" after cladding oxidation rate and fuel swelling rate were calibrated.

Fuel solid-swelling rate was upscaled in the calibration step (B) to solve the observed underestimations. Such a correction corresponds to strengthening the late-stage PCMI and *vice versa*. As fuel pellets are essentially rigid against cladding, the upward correction of swelling rate assures convergence of the matching procedure of the underpredicted cases as seen in **Fig. 4**.

In contrast, downscaling is often insufficient to solve the overpredictions on its own; since fuel pellets are modeled as cracked material, they push the cladding at PCMI but never pull nor extract. When an overprediction comes primarily from insufficient creep down of the cladding tube in the calculation, swelling rate correction does not work anymore. An upward correction of cladding creep rate is additionally required for completion of the matching procedure on the overpredicted cases. However, executing rod-by-rod corrections on cladding creep rate critically undermines meaningful comparison of stress or strain between the individual BWR rods, since

computation of such mechanical states entirely depends on the creep model adopted. For this reason, the calibration step (B) was skipped for the overpredicted cases, which entails overestimation of PCMI intensity. Note that the OS-1B rod always belonged to the underpredicted cases, as shown in **Fig. 4**, in the present work.

The present model considers the large-grain effect on fuel densification rate, namely limited densification of ADOPT^{TM} [11], in the case of the OS-1B rod. Still, among the underpredicted cases, the OS-1B rod required the largest upward correction of swelling rate at 24% whereas other cases only needed a maximum of 13%. As expressed in **Eq. A23** (see **Appendix**), in the updated HBS-induced-swelling model, the swelling rate is controlled by gas atom migration from the grain interior. Larger-grain fuel pellet tends to have a delayed gas atom accumulation in the HBS region, and thus have a delayed swelling by HBS-porosity evolution. This model feature may have cancelled the effect of suppressed densification to a degree. Actually the HBS-induced-swelling values are ~0.7% for OS-1B while ~1% for FK-10B and ~1.8% for LS-1B in the "As-predicted" results.

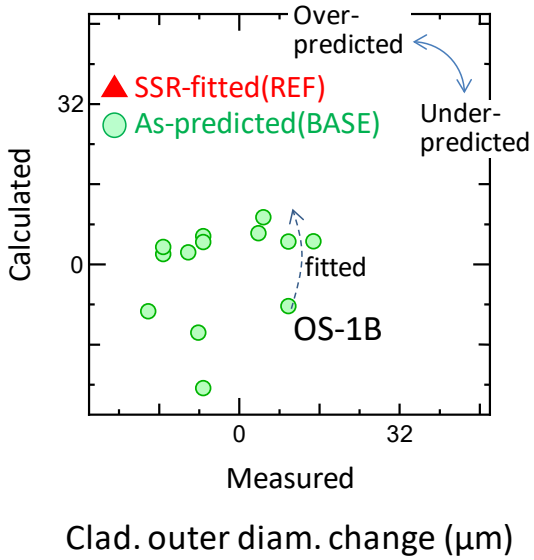

Figure 4 Cladding deformation fitted to measured values on BWR rods by modification of solid-swelling rate ("SSR"). The calibration step (B) started with the "BASE" model set and settled in the modified model set "REF".

Figures 5 compare cladding mechanical states computed by the model "REF" between the targeted BWR rods. They are from identical calculations to those plotted in **Fig. 4** as "SSR-fitted(REF)". In addition to cladding hoop-stress, which is known to be a relevant parameter to hydride orientation behaviors, the following creep parameter P_{CREP} was introduced as a creep-strain-based indicator of late-stage PCMI intensity:

$$P_{CREP} = \int \max\left(0, d\epsilon_{clad,hoop}\right) dBu \,, \qquad (1)$$

where $d\epsilon_{clad,hoop}$ is the hoop-direction creep-strain increment calculated for the cladding metallic layer and Bu is the corresponding burnup increment.

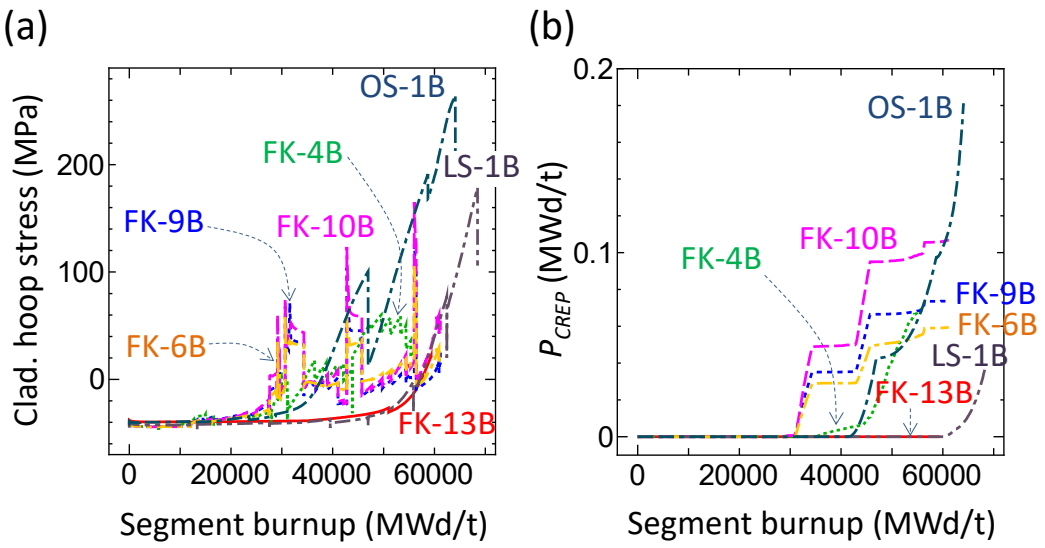

Figure 5 Comparison of base irradiation behaviors between different BWR rods: (a) cladding hoop stress level and (b) cladding creep parameter P_{CREP} by the model "REF". The sudden drops seen in **(a)** (for example around 44000 MWd/t of OS-1B) represent decreases in heating rate at the correspoinding burnups.

The hoop stress (see **Fig. 5(a)**) steeply increases with burnup in the late-stage of the OS-1B and LS-1B base irradiations, owing to HBS-porosity increase. The majority of FK rods are characterized by sharp stress increases at mid-burnup, which corresponds to the periods of high heating rate (~35 kW/m, **Table 1**). The OS-1B rod reached a higher stress level irrespective of the lower burnup compared to the LS-1B, and a lower heating rate level than the FK-10B. The parameter P_{CREP} shows a similar trend (see **Fig. 5(b)**).

3.2 Sensitivity analysis

Arborelius reported similar rod-diameter changes between an ADOPT^{TM} rod and a standard UO_2 rod in the burnup range of about 39–49 GWd/t [11]. Comparison of this observation and the underestimation trend of the OS-1B diameter discussed in Section 3.1 implies possibility of different swelling behavior of an ADOPT^{TM} rod from a standard UO_2 rod that emerges at higher burnup than 50 GWd/t. On the other hand, this observation may also raise doubts about the applicability of the calibration method above for scaling of fuel solid-swelling rates that uniformly effects the whole burnup period. Additional swelling of the OS-1B rod, implied in **Fig. 4**, may have occurred or accelerated only after 50 GWd/t. Another calculation set (named "REF_{HBS}") was prepared to check the significance of additional uneven swelling that scales HBS-induced-swelling rate in the step (B) (see **Fig. 2**) instead of the solid-swelling rate. The comparison with the model "REF" given in **Fig. 6** shows the timing of swelling enhancement has limited influence.

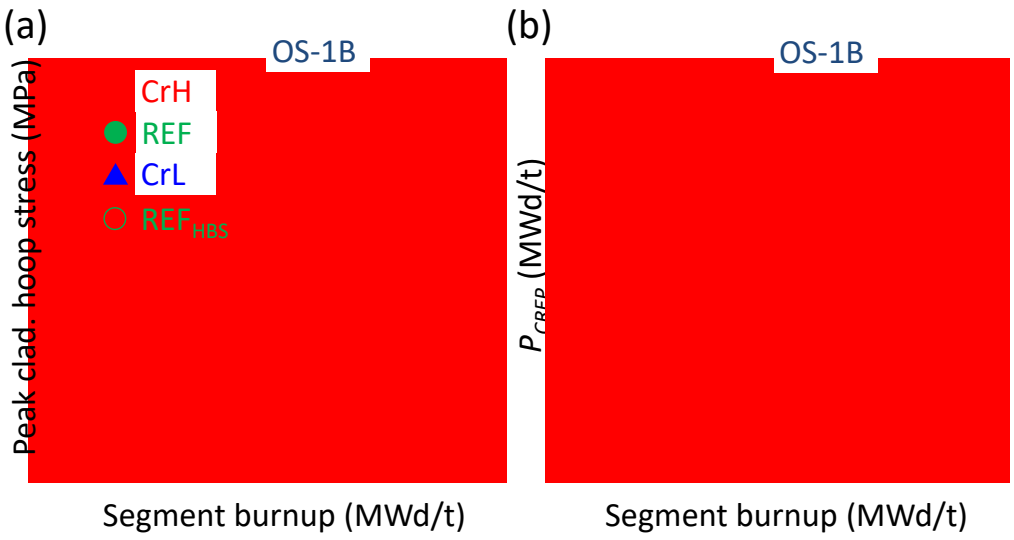

Figure 6 Summary of sensitivity analysis: (a) cladding hoop stress level and (b) cladding creep parameter P_{CREP} by the models "REF," "HBS," "CrH," and "CrL".

Figure 6 also presents the results from another set of sensitivity analyses: "CrH" and "CrL" with cladding creep rates scaled from "REF" to its 200% and 50%, respectively. Note that the creep-rate scaling does not mean a rod-by-rod parameter modification, which complicates the comparison as already discussed in Section 3.1. The scaling is applied to the every BWR rods uniformly, which corresponds to changing the base model set for the inverse-calculation procedure from "REF" to a different one with higher or lower creep rate. It is also important to note that since the "REF" model was a product of the validation process (see Section 2.2), the creep-rate scaling for "CrH" and "CrL" only worsenes agreement with the validation database. In other words, "CrH" and "CrL" are less supported by the PIE data. It was still thought valuable to confirm the exact impact of the cladding creep model in this analysis.

Both the peak stress level and the strain-based parameter P_{CREP} changed significantly with the creep-rate scaling as seen in **Fig. 6**. The decreasing trend of P_{CREP} with creep rate in **Fig. 6(b)** represents the delay of pellet/cladding contact owing to the mitigated creep down with lower creep rate. In the case of "CrL," the limited PCMI-induced cladding deformation lead to the moderate stress level as seen in **Fig. 6(a)** in spite of lower creep rate. The failure of the model "CrL" in detecting the saliency of the OS-1B rod in the P_{CREP} dimension indicates the critical importance of the accuracy of the cladding creep model in such a comparative analysis of the late-stage PCMI behaviors between different rods.

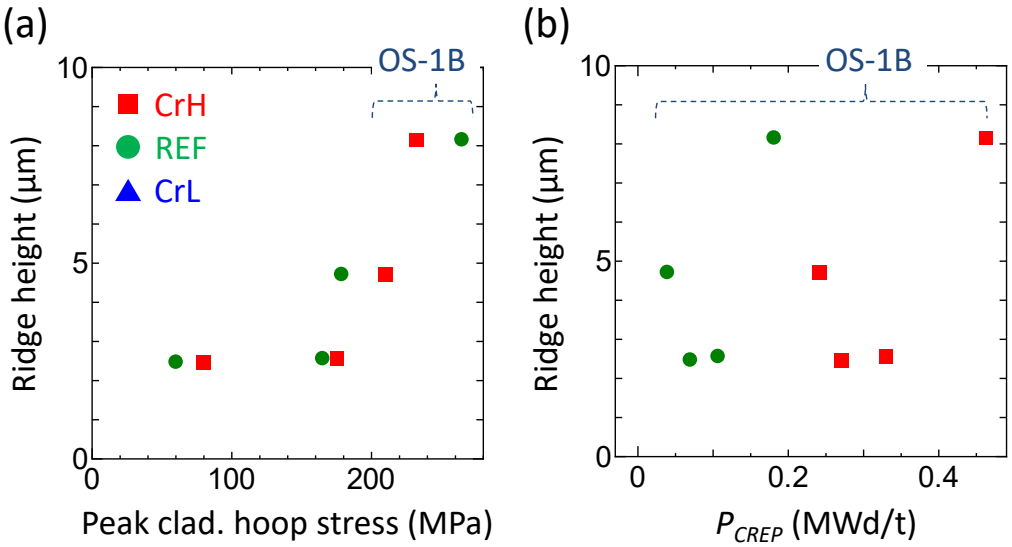

Figure 7 Correlations of calculated cladding mechanical states with measured ridge height: (a) cladding hoop stress level and (b) cladding creep parameter P_{CREP}. The ridge height was quantified based on cladding outer diameter profile measured in the PIEs.

Figure 7 correlates the calculated stress and P_{CREP} with the measured ridge height, which was roughly estimated based on the cladding outer diameter profile. A ridge height was calculated by subtracting cladding outer diameter at the valley of ridging profile from that at the top. This calculation was applied to all the ridges observed in the axial range corresponding to an NSRR test rod position, then the calculated ridge heights were averaged arithmetically for the plot. This geometric parameter is regarded as a possible indicator of the PCMI intensity since the ridging deformation should become prominent solely as a result of direct PCMI. The overall consistency, namely the positive correlation in the figure, confirms the validity of the mechanical state parameters to represent the late-stage PCMI intensity, except in the case of "CrL".

3.3 PCMI-failure map for BWR rods

Figure 8 correlates the cladding mechanical state parameters calculated by the model "REF" with cladding hydrogen content measured at the vicinities of the NSRR test rod positions. The majority of the plotted BWR data was obtained by RIA-simulated tests at room temperature, except FK-10 and -12 which were performed at around 80 C˚. As implied in the above discussion, both charts discriminate the OS-1, specifically the PCMI failure at the lowest fuel enthalpy increase in all the BWR test cases ever performed, from other BWR-fuel failures. On the whole, the failure limit values appear to form a downward trend toward the upper-right corners, which is qualitatively expected. This trend, in addition to the saliency of the OS-1 rod, supports the explanation of the OS-1 failure by the contribution of radial hydrides and provides an interpretation that the fuel segment, from which the OS-1 test rod was cut out, experienced relatively intense PCMI loading and that the associated tensile state accelerated formation of radial hydrides in the cladding metallic layer.

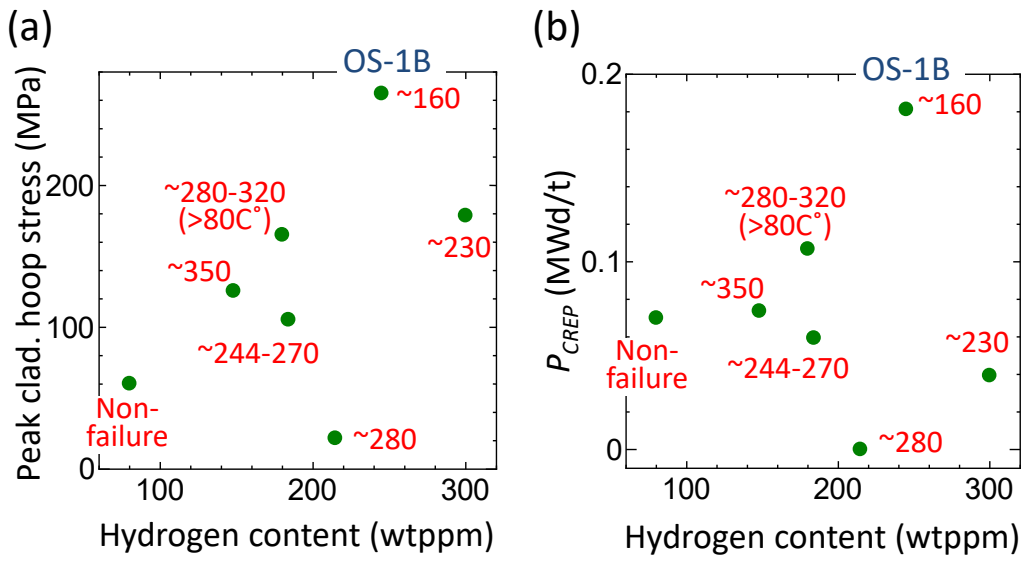

Figure 8 Correlations of calculated cladding mechanical states with measured hydrogen content: (a) cladding hoop stress level and (b) cladding creep parameter P_{CREP}. Numbers embedded in the figures present rounded values of fuel enthalpy increases at failure observed in the corresponding RIA-simulated tests.

Finally, we also tried a preliminary quantification of the hydride morphology features presented in **Fig. 1**, which originally motivated this work. The image analysis binarized the metallography image, linearized the objects which were recognized as hydride precipitates after binarization, and then summated the radial components of the line objects $L_{RH,eff}$ as

$$L_{RH,eff} = \sum_{ih=1}^{N_H} L_{H,ih} cos\theta_{ih} \ , \qquad (2)$$

where N_H and L_H [μm] are the number and the length of the line object representing a part of a hydride precipitate, respectively, and θ is the angle of the line object from the radial direction. The image analysis gave $L_{RH,eff}$ = ~3200 for the OS-1 sample (**Fig. 1(a)**) and ~2100 for the LS-1 sample (**Fig. 1(b)**), which appears consistent with the both relations of evaluated cladding mechanical states and the failure limits between the two test cases seen in **Fig. 8**. Here it should be emphasized, however, that such a reductional approach entails all the strong dependencies on specimen sampling position, etching conditions, operator effects, etc., which are inherent in metallographic observation process. Much more evaluations on different specimens are indispensable to conclude whether the present coincidence of $L_{RH,eff}$ with other parameters reflects the importance of radial-hydride effect or just a result of data scatter.

4. Conclusion

The comparative base irradiation analysis using FEMAXI-8 code on the BWR fuel rods thus far subjected to the RIA-simulated tests at the NSRR, indicated that the ADOPT^{TM}-type BWR fuel rod subjected to the test OS-1 had very likely experienced relatively intense PCMI loading during the base irradiation compared to other BWR rods. The analysis strongly suggests that the

fuel pellets swelled at a higher rate during the base irradiation of the OS-1 rod, while the reason for said swelling behavior in this specific rod is unclear. This conclusion is consistent with the preferential orientation of hydrides along the radial direction of the cladding tube and thus supports the hypothesis that radial hydrides contributed to PCMI failure of the OS-1 rod at the lowest fuel enthalpy increase in all of the BWR tests ever performed.

Although such an analytical approach may help to discriminate fuel rod designs or irradiation conditions that increase risk of PCMI failure assisted by radial-hydride formation, it only allows a conservative estimation of indirect mechanical state parameters; they should not be the sufficient condition but rather a part of necessary conditions of radial-hydride formation such as stress state, hydrogen content, temperature dependent hydrogen solubility, thermal cycles, and cladding material properties. The degree of radial-hydride contribution needs to be clarified in a quantitative manner. At this moment, any conclusion on ADOPT^{TM}-specific effects, particularly under transient conditions, has not been reached at all. Possible contributions of both the pellet-side and cladding-side effects should be evenly and carefully assessed through follow-up PIEs and RIA-simulated tests that will be conducted in the near future.

Appendix. Model updates to improve prediction of cladding deformation during base irradiation

This appendix describes modifications of the previous work [6,7] that were primarily made to improve the predictive performance on cladding deformation during base irradiation.

(1) The evolution of fuel swelling S_{HBS} due to the development of HBS porosity p_{HBS} during time step Δt [s] is computed as follows:

$$\Delta S_{HBS,ix} = F_{HBSvol} \Delta p_{HBS} f_{aniso,ix} \,, \tag{A1}$$

$$F_{HBSvol} = \varepsilon_{pol,kjma} \,, \tag{A2}$$

$$\varepsilon_{pol,kjma} = 1 - \exp\left(-(1 - \frac{(d_{grain,init} - 10)}{2(60-10)})(\frac{Bu_{kjma}}{MP_1})^{MP_2}\right), \tag{A3}$$

$$\Delta Bu_{kjma} = \varphi T_{ref,kjma} \Delta t \,, \tag{A4}$$

$$T_{ref,kjma} = \max\left(0, \min\left(1, \frac{MP_3 - T_f}{MP_3 - MP_4}\right)\right), \tag{A5}$$

$$\Delta p_{HBS} = V_{GB} C_{GB} \,, \tag{A6}$$

$$V_{GB} = 4/3\pi R_{GB}^3 \,, \tag{A7}$$

$$R_{GB} = M_{GB}/C_{GB} \,, \tag{A8}$$

$$f_{aniso,ix} = \exp(MP_5 \sigma_{ix}) / \textstyle\sum_{ix} \exp(MP_5 \sigma_{ix}) \,, \tag{A9}$$

where ix denotes the directions in a fuel rod system (r, θ, z), F_{HBSvol} and $\varepsilon_{pol,kjma}$ are the volume fraction of polygonized fuel matrix region, f_{aniso} is the anisotropy factor, $d_{grain,init}$ [μm] is the initial fuel-grain size, Bu_{kjma} [FIMA] is the effective burnup, φ [cm^{-3}s^{-1}] is the fission rate, $T_{ref,kjma}$ [K] is the reference temperature, T_f [K] is the fuel element temperature, V_{GB} [cm^3] is the single gas bubble volume, C_{GB} = 1.3×10^{11} [cm^{-3}] is the initial and constant gas bubble density, R_{GB} [cm] is the HBS-gas-bubble radius, M_{GB} [cm^{-2}] is the quantity called bubble moment, and σ [MPa] is fuel stress. Model parameters MP_{1-5} are set to be 0.068, 4, 1073.0, 723.0, and 1.0, respectively. The formulation of fuel matrix polygonization is based on Khvostov's work [13].

(2) The time evolution of the HBS state variable M_{GB} is treated by the following rate equations:

$$\frac{dM_{GB}}{dt} = \frac{dM_{GB,T}}{dt} + \frac{dM_{GB,V}}{dt} + \frac{dM_{GB,D}}{dt} \,, \tag{A10}$$

where $\frac{dM_{GB,T}}{dt}$, $\frac{dM_{GB,V}}{dt}$, and $\frac{dM_{GB,D}}{dt}$ [cm^{-2}s^{-1}] denote the contributions of fuel matrix transformation to the polygonized structure, vacancy emission/absorption, and dislocation punching driven by gas bubble pressure, respectively.

The 1st term is formulated as:

$$\frac{dM_{GB,T}}{dt} = C_{GB} \frac{\left(\frac{3}{4\pi} \frac{p_{HBS,T}}{C_{GB}}\right)^{1/3} - R_{GB}}{\Delta t} \,, \tag{A11}$$

$$p_{HBS,T} = \frac{V_{GB}C_{GB}F_{HBSvol} + p_{NP}\Delta F_{HBSvol}}{F_{HBSvol} + \Delta F_{HBSvol}}, \quad \text{(A12)}$$

where $p_{HBS,T}$ is the porosity of the newly generated polygonized fuel matrix, and p_{NP} is the porosity of the non-polygonized fuel matrix.

The 2nd term is formulated as:

$$\frac{dM_{GB,V}}{dt} = C_{GB}\frac{dR}{dt}\min\left(1, \left(\frac{F_{HBSvol} - 10^{-4}}{0.01 - 10^{-4}}\right)^2\right), \quad \text{(A13)}$$

$$\frac{dR}{dt} = \frac{1}{R_{GB}}\left(D_v C_{vi} - D_v C_{vu}\exp\left(\left(P_{hyd} + \frac{2\gamma}{R_{GB}} - P_{GB}\right)\omega/(kT_f)\right)\right), \quad \text{(A14)}$$

where $D_v = 10^{-3}\exp(-2.4/(kT_f))$ [cm^{2}s^{-1}] is the vacancy diffusion coefficient, C_{vi} [cm^{-3}] is the vacancy concentration under irradiation by White [14] (proposed for calculation of irradiation-enhanced fission gas diffusion), C_{vu} [cm^{-3}] is the thermal-equilibrium vacancy concentration computed by Griesmeyer's approach [15], P_{hyd} [eVcm^{-3}] is the hydrostatic pressure, γ [eVcm^{-2}] is the surface energy, P_{GB} [eVcm^{-3}] is the HBS-gas-bubble pressure, ω [cm^3] is the atomic volume, and k [eV/K] is the Boltzman constant.

The 3rd term adopts the discussion by Une [16] on the role of dislocation punching from the HBS gas bubble and is formulated as:

$$\frac{dM_{GB,D}}{dt} = 10^{-7}\exp\left(\min\left(15, \left(P_{GB2}f_{irrad} + P_{hyd,eff} - P_{DP}\right)\right)\right), \quad \text{(A15)}$$

$$P_{GB2} = k_2 T_f N_{atm}/V_{GB}, \quad \text{(A16)}$$

$$N_{atm} = C_{HBS,atm}/C_{GB}, \quad \text{(A17)}$$

$$f_{irrad} = \frac{1}{1 + 1.1\times10^{-10}\pi\lambda(10^{-6} + R_{FS})^2\varphi C_{GB}}, \quad \text{(A18)}$$

$$P_{hyd,eff} = \begin{cases} S_{avg} & for\ S_{avg} > -35\ MPa \\ -\left(35 + 0.2\left(\left|S_{avg}\right| - 35\right)\right) & for\ S_{avg} \le -35\ MPa \end{cases}, \quad \text{(A19)}$$

$$P_{DP} = 0.7\left(\frac{Gb}{R_{GB}} + \frac{\gamma_2}{R_{GB}}\right), \quad \text{(A20)}$$

where P_{GB2} [MPa] is the HBS-gas-bubble pressure, f_{irrad} is an empirical pressure-depression factor by irradiation, $P_{hyd,eff}$ [MPa] is the effective hydrostatic stress used for the calculation of the dislocation punching rate, P_{DP} [MPa] is the minimum gas bubble pressure required for the occurrence of dislocation punching [16], k_2 [JK^{-1}] is the Boltzman constant, N_{atm} is the number of fission gas atoms belonging to a single HBS gas bubble, $C_{HBS,atm}$ [cm^{-3}] is the HBS gas-atom concentration per unit HBS volume, $\lambda = 6 \times 10^{-4}$ [cm] is the range of fission fragments, $R_{FS} = 10^{-7}$ [cm] is the radius of the fission spike, S_{avg} [MPa] is the average stress, G = 79000 [MPa] is the fuel shear modulus, $b = 3.9 \times 10^{-10}$ [m] is the Burgers vector, and γ_2 [Jm^{-2}] is the surface energy.

(3) Evolution of the HBS gas-atom concentration $C_{HBS,atm}$ during time step Δt is computed as follows:

$$C_{HBS,atm} = (C_{HBS,atm,prv}\varepsilon_{pol,kjma,prv} + \Delta J_{HBS})/\varepsilon_{pol,kjma}\,, \tag{A21}$$

$$\Delta J_{HBS} = \Delta J_{HBS,dif} + \Delta J_{HBS,T}\,, \tag{A22}$$

$$\Delta J_{HBS,dif} = \Delta J_{OUT}\varepsilon_{pol,kjma}\,, \tag{A23}$$

where the subscript prv denotes the value at the beginning of the time step Δt, ΔJ_{HBS} [cm^{-3}] is the gas migration to the HBS region during Δt per unit fuel element volume, $\Delta J_{HBS,dif}$ and $\Delta J_{HBS,T}$ are contributions of diffusing gas atoms from the non-polygonized region and those involved in the polygonization process, respectively, and ΔJ_{OUT} [cm^{-3}] is the gas-atom diffusion flux from the non-polygonized grain-interior region.

(4) The intra-grain gas-atom diffusion calculation [17], which determines ΔJ_{OUT}, adopts the following formulation of gas-atom diffusion coefficient $D_{gas,atm}$ [cm^{2}s^{-1}]:

$$D_{gas,atm} = (D_{Matzke} + 0.5\times 10^{-22}\varphi^{0.3})f_{dif,pol}\,, \tag{A24}$$

$$f_{dif,pol} = \left(\min\left(d_{grain,init}, 20\right)/d_{grain,eff}\right)^{n_{dif,pol}}, \tag{A25}$$

$$d_{grain,eff} = \min(d_{grain,kjma}, d_{grain,mtrg})\,, \tag{A26}$$

$$n_{dif,pol} = \begin{matrix} 1 & for\ d_{grain,mtrg} < d_{grain,kjma} \\ 3 & for\ d_{grain,mtrg} \geq d_{grain,kjma} \end{matrix}, \tag{A27}$$

$$d_{grain,kjma} = \frac{0.35 d_{grain,init}}{d_{grain,init}\varepsilon_{pol,kjma} + 0.35\left(1-\varepsilon_{pol,kjma}\right)^{2/3}}, \tag{A28}$$

$$d_{grain,mtrg} = \frac{0.40 d_{grain,init}}{d_{grain,init}\varepsilon_{pol,mtrg} + 0.40\left(1-\varepsilon_{pol,mtrg}\right)^{2/3}}, \tag{A29}$$

$$\varepsilon_{pol,mtrg} = 1 - \exp\left(-(1-\tfrac{(d_{grain,init}-10)}{2(60-10)})(\tfrac{Bu_{mtrg}}{0.04})^3\right), \tag{A30}$$

$$\Delta Bu_{mtrg} = \varphi T_{ref,mtrg}\Delta t\,, \tag{A31}$$

$$T_{ref,mtrg} = \max\left(0, \min\left(1, \frac{1503 - T_f}{1503-1223}\right)\right) f_{lowT}\,, \tag{A32}$$

$$f_{lowT} = \begin{matrix} 0.1 & for\ T_f \leq 773 \\ 0.1 + (1-0.1)\dfrac{\left(T_f - 773\right)}{1123-773} & for\ 773 < T_f \leq 1123 \\ 1.0 & for\ 1123 < T_f \end{matrix}, \tag{A33}$$

where D_{Matzke} [cm^{2}s^{-1}] corresponds to the coefficient adopted in the previous work [7], $f_{dif,pol}$ is the correction factor to take polygonization into account, $d_{grain,eff}$ [μm] is the effective grain size to be simulated by the factor $f_{dif,pol}$, $d_{grain,kjma}$ and $d_{grain,mtrg}$ [μm] are the effective grain sizes affected by polygonization in low-temperature and mid-temperature regions,

respectively, and $\varepsilon_{pol,mtrg}$, ΔBu_{mtrg}, $T_{ref,mtrg}$, and f_{lowT} are empirically determined auxiliary variables to represent the burnup effect on gas atom diffusion in the mid-temperature region, adopting a similar formulation to the one applied to the low-temperature polygonization $\varepsilon_{pol,kjma}$.

(5) The correlation of the vacancy diffusion coefficient used for the calculation of grain boundary gas-bubble porosity was re-calibrated from [7] as:

$$D_{v,GB} = \begin{cases} 9.0 \exp\left(-\frac{57520}{T_f}\right) & for\ T_f \le 1273 \\ \max\left(9.0 \exp\left(-\frac{57520}{T_f}\right), 8.38 \times 10^{-5} \exp\left(-\frac{45000}{T_f}\right)\right) & for\ 1273 < T_f \end{cases}, \quad \text{(A34)}$$

and the correction factor previously introduced [6,7] to take account of burnup effect on $D_{v,GB}$ was omitted in the present update. The formulation of the fraction of gas atoms in the grain boundary face that contributes to the pressure of face gas bubbles F_{cntrb} was modified as well:

$$F_{cntrb} = \frac{1}{1 + 3 \times 10^{-27} \varphi / D_{gas,atm}}, \quad \text{(A35)}$$

by introducing parameters that are likely more relevant to the resolution process, instead of burnup [6]. The hydrostatic pressure calculated in the mechanical model of FEMAXI-8 acts on the grain boundary gas bubbles with mitigation by a factor of 0.6.

(6) The transient gas-bubble migration rate from the grain interior to the boundary by biased migration was suppressed by a factor of 0.1 from the previous work [6].

(7) The fuel pellet thermal-expansion model was changed to the widely used MATPRO model [18] from the previous work [7].

(8) The fuel pellet mechanical relocation assumed at the first power rise in an irradiation history was modified to 1%, which is up from 0.6% that is adopted in previous work [7].

(9) The progress of pellet-cladding chemical bonding F_{bond} is evaluated by:

$$\Delta F_{bond} = \frac{P_{PCMI} \Delta t}{10000} \times \frac{10^{-6}}{3600}, \quad \text{(A36)}$$

where P_{PCMI} [Pa] is the PCMI (contact) pressure, and F_{bond} = 1.0 corresponds to the completion of bonding formation.

(10) The parameter β for the fuel hot-press term taken into account in the calculation of the equivalent stress [17] used in the fuel creep model was modified to 0.002:

$$\sigma_{eq} = \sqrt{\sigma_{eq,0}^2 + 3\beta\sigma_{avg}^2}, \quad \text{(A37)}$$

where σ_{eq} [Pa] is the fuel equivalent stress, $\sigma_{eq,0}$ [Pa] is the fuel equivalent stress without the hot-press effect, and σ_{avg} [Pa] is the fuel average stress.

(11) Under relatively low-temperature (below 1273 K) and low equivalent-stress (50 MPa) conditions, the fuel creep model [17,7] is inactivated.

(12) The cladding creep model adopts the MATPRO-09 model [18] with scaling factors of 1.3 for stress-relief-annealed cladding and 0.5 for RX-annealed cladding.

Acknowledgments

A part of the RIA-simulated experiments and the post-irradiation examinations analyzed in this study was performed under the research entrusted by Secretariat of Nuclear Regulation Authority. The test fuels for the FK-series experiments were provided by Tokyo Electric Power Company Holdings, Inc.

References

[1] Mihara, T., Udagawa, Y., Amaya, M., Taniguchi, Y., and Kakiuchi, K., "BEHAVIOR OF LWR FUELS WITH ADDITIVES UNDER REACTIVITY-INITIATED ACCIDENT CONDITIONS," Proc. Topfuel2019, Paper No. 30015, Seattle (2019).

[2] Sugiyama, T., Umeda, M., Fuketa, T., Sasajima, H., Udagawa, Y., and Fumihisa, N., "Failure ofhigh burnup fuels under reactivity-initiated accidentconditions," Ann. Nucl. Energy, **36**, pp. 380–385, (2009).

[3] Proceedings of the topical meeting on ria. France:Nuclear Energy Agency, OECD; 2003, Report NEA/CSNI/R(2003)8/VOL1. "Japanese Nuclear Safety Commission Regulatory Guidelines," p961-1026 (1998).

[4] Papin, J., Cazalis, B., Frizonnet, JM., Desquines, J., Lemoine, F., Georgenthum, V., Lamare, F., and Petit, M., "SUMMARY AND INTERPRETATION OF THE CABRI REP-Na PROGRAM," Nucl. Technol., **157**, pp. 230–250, (2007).

[5] Hardie, D., Y., and Shanahan, N., "Stress reorientation of hydrides in zirconium−2.5% niobium," J. Nucl. Mater., **55**, pp. 1–13, (1975).

[6] Udagawa, Y., and Amaya, M., "Model updates and performance evaluations on fuel performance code FEMAXI-8 for light water reactor fuel analysis," J. Nucl. Sci. Technol., **56**, pp. 461–470, (2019).

[7] Udagawa, Y., Yamauchi, A., Kitano, K., and Amaya, M., "Development of fuel performance code FEMAXI-8—model improvements for light water reactor fuel analysis and systematic validation—," JAEA-Data/Code 2018-016, (2018).

[8] Udagawa, Y., Sugiyama, T., and Amaya, M., "Thresholds for failure of high-burnup LWR fuels by Pellet Cladding mechanical interaction under reactivity-initiated accident conditions," J. Nucl. Sci. Technol., doi.org/10.1080/00223131.2019.1637795.

[9] Nakamura, T., Kusagaya, K., Fuketa, T., and Uetsuka, H., "Highburnup BWR fuel behavior under simulated reactivity-initiated accident conditions," Nucl. Technol., **138**, pp. 246–259, (2002).

[10] Nakamura, T., Fuketa, T., Sugiyama, T., and Sasajima, H., "Failure thresholds of high burnup BWR fuel rods under RIA conditions," J. Nucl. Sci. Technol., **41**, pp. 37–43, (2004).

[11] Arborelius, J., Backman, K., Hallstadius, L., et al., "Advanced Doped UO_2 Pellets in LWR Applications," J. Nucl. Sci. Technol., **43**, pp. 967–976, (2006).

[12] url:http://warp.da.ndl.go.jp/info:ndljp/pid/8405841/www.jnes.go.jp/gijyutsu/seika/, last-accessed: 2019-11-22.
[13] Khvostov, G., Mikityuk, K., and Zimmermann, MA., "A model for fission gas release and gaseous swelling of the uranium dioxide fuel coupled with the FALCON code," Nucl. Eng. Design, **241**, pp. 2983–3007, (2011).
[14] White, RJ. and Tucker, MO., "A new fission-gas release model," J. Nucl. Mater., **118**, pp. 1–38(1983).
[15] Griesmeyer, JM., Ghoniem, NM., and Okrent, D., "A dynamic intragranular fission gas behavior model," Nucl. Eng. Design, **55**, pp. 69–95 (1979).
[16] Une, K., Kashibe, S., and Takagi, A., "Fission gas release behavior from high burnup UO2 fuels under rapid heating conditions," J. Nucl. Sci. Technol., **43**, pp.1161–1171 (2006).
[17] Suzuki, M., Saitou, H., Udagawa, Y., and Nagase, F., "Light Water Reactor Fuel Analysis Code FEMAXI-7; Model and Structure," JAEA-Data/Code 2013-005, (2013).
[18] MacDonald, PE. and Thompson, LB., "MATPRO — VERSION 09 A HANDBOOK OF MATERIALS PROPERTIES FOR USE IN THE ANALYSIS OF LIGHT WATER REACTOR FUEL ROD BEHAVIOR," TREE-NUREG-1005, US Nuclear Regulatory Commission, Washington, DC, (1976).